energy&fuels

pubs.acs.org/EF

Article

Investigating the Interaction between Ilmenite and Zinc for Chemical Looping

Ivana Staničić,* Emil Ola Lidman Olsson, Hao Wu, Peter Glarborg, Iñaki Adánez-Rubio, Henrik Leion, and Tobias Mattisson

Cite This: *Energy Fuels* 2023, 37, 7856−7870

Read Online

ACCESS | Metrics & More | Article Recommendations | Supporting Information

ABSTRACT: The iron and titanium oxide ilmenite is a benchmark oxygen carrier for chemical looping combustion (CLC) and oxygen carrier-aided combustion (OCAC). Both of them are combustion technologies for biomass and waste fuels with lower emissions and low costs for carbon capture. Here, the interaction between the ash component zinc and oxygen carrier ilmenite is studied in a two-staged vertical tube reactor. Three types of ilmenites—Norwegian rock ilmenite, synthesized ilmenite, and ilmenite extracted after 200 h of OCAC in a full-scale fluidized bed unit—were exposed to gas-phase Zn and $ZnCl_2$. Following the exposure, samples were analyzed concerning morphology, chemical distribution, composition, and crystalline phases. The observations were complemented with thermodynamic equilibrium calculations. It is observed that the iron-rich layer formed on the external surface of rock ilmenite after activation promotes the reaction with both gaseous zinc compounds, with zinc ferrite formed in the external Fe-rich layer. In contrast, ilmenite with no segregation of Fe and Ti showed to interact less with zinc species. Metallic Zn penetrated the particles, while the interaction depth was shallow with $ZnCl_2$ for all investigated ilmenite oxygen carriers. The gaseous conditions, particle ash layer composition, and iron availability are shown to play an important role in the interaction between zinc compounds and ilmenite particles. Based on these results, interaction mechanisms for Zn and $ZnCl_2$ are proposed. This interaction could have environmental implications for the toxicity of ash streams from waste combustion in addition to possibilities for Zn recycling.

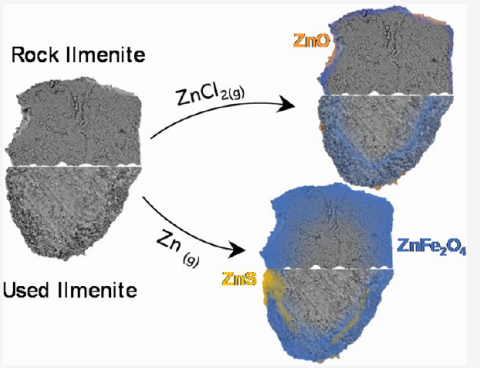

1. INTRODUCTION

To meet climate targets, significant reductions of anthropogenic greenhouse gas emissions are necessary, in addition to large-scale negative emissions of CO_2 from the atmosphere.[1−4] One technology that prohibits the release of CO_2 into the atmosphere is carbon capture and storage (CCS), and one related technology that removes CO_2 from the atmosphere is bio-energy with carbon capture and storage (BECCS). BECCS is included in almost all access mitigation scenarios for meeting climate goals.[5] BECCS is based on capturing CO_2 from biogenic sources, resulting in a net negative flow of CO_2 from the atmosphere.[6] There are some issues to deal with when implementing CO_2-capture technologies in existing plants. For example, fuels are commonly combusted using air, and consequently, two-thirds of the flue gas is composed of nitrogen. The nitrogen and CO_2 need to be separated before capture, and there are high costs associated with both the separation equipment and energy input required.[7]

One technology with inherent CO_2 separation is chemical looping combustion (CLC). In recent years, the use of biomass in CLC has gained interest as a BECCS option.[8−10] CLC is composed of two interconnected fluidized bed reactors, the air reactor (AR) and fuel reactor (FR), and their schematics are presented in Figure 1a. The bed material used in these fluidized beds is metal oxide, so-called oxygen carriers (OCs), the cornerstone of CLC. The purpose of the OC is to transfer heat and oxygen from the AR to the FR. The AR is fluidized with air and is where the OC is oxidized before being transported to the FR. In the FR, oxygen is released, and the fuel is converted to CO_2 and H_2O in a nitrogen-free environment. After condensation of H_2O, a highly concentrated stream of CO_2 is obtained, suitable for CCS.

An additional benefit of OCs is that they can easily replace the traditionally used bed materials in existing fluidized bed facilities.[11] Replacing the bed material in such facilities with OCs will even out both the temperature and oxygen distribution in the reactor, which can have several benefits concerning lowering emissions and reducing corrosion.[11,12] The metal oxides are oxidized and reduced in the same reactor

Received: March 30, 2023
Revised: May 8, 2023
Published: May 18, 2023

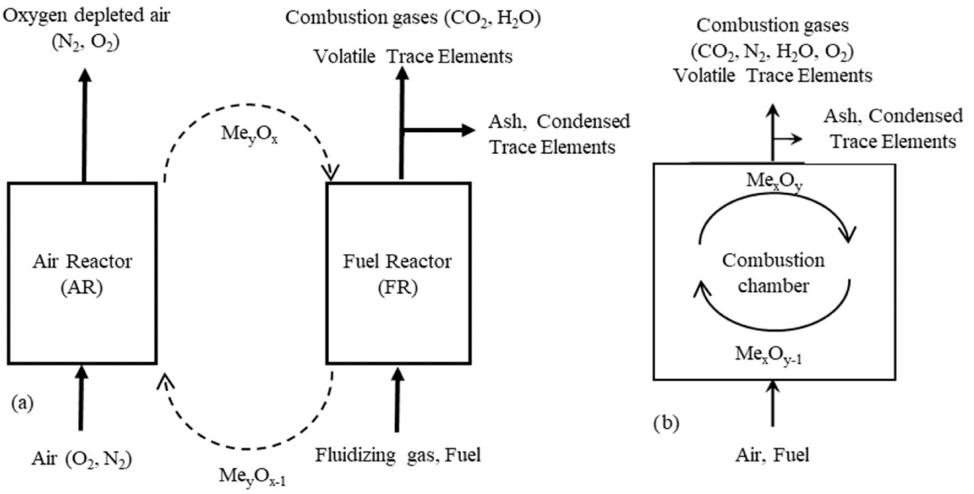

Figure 1. (a) Schematic description of chemical looping combustion (CLC) and (b) oxygen carrier-aided combustion (OCAC).

and consequently releasing heat and oxygen in deficient areas of the boiler. This process is referred to as oxygen carrier-aided combustion (OCAC), and the schematic of this process is presented in Figure 1b.

The conditions in the FR in CLC and the combustion chamber in OCAC are different. In OCAC, the fluidizing gas is air. However, in CLC, the FR is commonly fluidized using H_2O, or recirculated CO_2. Due to this, the bed material and gaseous components are expected to be at a higher reduced state in the FR during CLC, compared to OCAC. Zinc, for example, has been observed in the form of gaseous zinc chloride in oxidizing environments in fluidized beds[13] and conditions endured in OCAC.[14] However, the release of zinc in the form of zinc gas could be relevant in reducing conditions, encountered in the FR during CLC.[15]

Global waste generation is expected to increase from 2.01 billion tons (2016) to 3.40 billion tons by 2050.[16,17] The worldwide growth in waste generation is primarily due to the rise in population, urbanization, and industrialization.[16,18] With population and economic growth, the global energy demand will increase and require a steady supply of affordable renewable energy with minimum environmental impacts. Municipal solid waste contains a considerable fraction of biomass and is an attractive fuel.[19] Burning waste and biomass to generate heat and electricity while capturing CO_2 can lead to net negative emissions, a field where BECCS could be widely applied. Here, CLC is an attractive option as the cost and energy penalty associated with CO_2 capture are among the lowest compared to other technologies.[9] To understand the effect of oxygen carriers on fuel conversion and ash behavior knowledge from technologies where oxygen carriers are currently utilized, such as OCAC, is highly valuable. This is especially true since OCAC has been utilized at an industrial scale for the conversion of different waste fractions. Studies on OC from OCAC of waste have shown that the behavior of heavy metals is affected by the presence of OCs and that some heavy metals can accumulate in the OC.[20]

A metal oxide needs to fulfill several criteria to be considered a suitable OC. These criteria impose requirements on the OC to have high oxygen transport capacity, high reactivity toward fuel and oxygen, high mechanical strength, resistance to attrition and agglomeration, be abundant, and have relatively low cost. One example is ilmenite concentrate, hence referred to as rock ilmenite, which is obtained after crushing and processing the iron and titanium rich mineral ore. Ilmenite fulfills the OC requirements considerably and has therefore been extensively studied in academia and also implemented in industrial applications.[11,12,21−26] Considering the knowledge obtained around ilmenite as an OC and its wide implementation, it is considered a benchmark oxygen carrier. Ilmenite utilized in the combustion of biomass and waste has been studied concerning major ash-forming elements[27−29] and heavy metals.[14,20] With time, ilmenite particles will exhibit increased porosity accompanied by cracks in the particles,[30] along with segregation of iron to the particle surface and enrichment of titanium in the particle core.[31] The most recent study used thermodynamic equilibrium calculations to illustrate possible pathways for important heavy metals during CLC of biomass and waste. Zinc is expected to be present in the FR as Zn (g) and in the solid phase as $ZnFe_2O_4$, ZnS, or zinc silicates.[15] The spinel, $ZnFe_2O_4$, has been observed in ilmenite experimentally after OCAC operation.[20] However, the behavior of zinc under CLC conditions and the mechanism of zinc ferrite formation during OCAC is not completely understood. Considering that the zinc fraction in certain waste fuels could be high and that it has a combination of high economic value and environmental characteristics that make it unsuitable to deposit in landfills, it is important to obtain a better understanding of the fate of zinc in CLC and OCAC.

In this study, the oxygen carrier ilmenite is investigated for its interaction with gaseous zinc compounds. The goal is to gain a better fundamental understanding of the chemistry behind the interactions of gaseous Zn compounds and ilmenite particles and to determine the influence of particle properties. To achieve this, ilmenite samples have been investigated in a vertical tube reactor along with two common gaseous zinc compounds: $ZnCl_2$ and Zn. The samples were analyzed concerning morphology, chemical distribution, and crystalline phases, and the observations were complemented with thermodynamic equilibrium calculations. The purpose is to examine the interaction and propose a mechanism based on the influence of activation and the influence of an existing ash layer.

2. MATERIALS

Three different types of ilmenite oxygen carriers were used in this work; synthesized ilmenite, rock ilmenite, and rock ilmenite used in

https://doi.org/10.1021/acs.energyfuels.3c01052
Energy Fuels 2023, 37, 7856−7870

OCAC of biomass and waste. The properties of the oxygen carriers are presented in Table 1. The synthesized ilmenite was produced at

Table 1. Properties of the Studied Oxygen Carriers

acronym	oxygen carrier	BET surface area [m^2/g]	Fe/Ti molar ratio	particle size [μm]	origin
OC1a	synthesized ilmenite	0.617	1.1:1	100−200	ICB-CSIC
OC1b	activated synthesized ilmenite	0.636			
OC2a	rock ilmenite	0[a]	1.1:1	150−200	Titania A/S
OC2b	activated rock ilmenite	0.236			
OC3	used ilmenite	0.254	1.2:1	90−250	20, 30

[a]Results obtained were similar to the blank test.

Instituto de Carboquímica-Spanish Research Council (ICB-CSIC) in a small granulator (high shear mixing granulator from Eirich) with an iron-to-titanium molar ratio of 1.1:1. The raw materials used to prepare synthesized ilmenite oxygen carrier was TiO_2 (Acros Organics, ≥98 wt % purity) and Fe_2O_3 (Acros Organics, ≥95 wt % purity). The synthesized ilmenite (OC1a) was sieved to obtain particles in the range of 100−200 μm and calcined at 1100 °C in air for 6 h. The rock ilmenite is supplied by Titania A/S and has been calcined in air at 950 °C for 12 h. To understand the influence of the ash layer on the interaction with zinc, used ilmenite (OC3) was extracted from an industrial fluidized bed unit after 200 h of OCAC operation with recovered waste wood and wood chips. The boiler was operated at 850 °C and the samples have been investigated previously concerning kinetics, trace elements, and magnetic properties.[20,30] With this selection of samples, it is possible to study the interaction between zinc and pure ilmenite components and gradually increase the complexity.

Relevant zinc compounds were selected based on their expected form during OCAC and CLC of waste.[14,15,20] Previous studies have established the release of zinc chloride in oxidizing environments in fluidized beds[13] and those encountered during OCAC conditions.[14] However, the release of zinc in the form of zinc gas could be relevant in reducing conditions, for example, encountered in the FR during CLC.[15] Thus, the gas−solid interaction between ilmenite and zinc in OCAC and CLC conditions was in this work investigated using the two important Zn compounds: zinc chloride (≥99 wt % purity) and metallic zinc powder (≥96 wt % purity). The solid compounds were heated under controlled conditions to obtain species in the gas phase that can react with the solid ilmenite in a gas−solid reaction.

2.1. Oxygen Carrier Activation. It is known that ilmenite gains reactivity when repeatedly exposed to cycles of oxidizing and reducing conditions. This process is referred to as activation and is accompanied by structural changes such as the formation of cracks and iron migration to the surface.[32,33] To study the influence of oxygen carrier activation on the interaction with zinc samples OC1a and OC2a were treated in consecutive cycles with alternating reducing and oxidizing conditions in a fluidized bed batch reactor. A process that was done without the presence of zinc compounds. The quartz reactor used for this has an outer/inner diameter of 22/20 mm and a height of 820 mm. A porous quartz plate was used as support for 15 g of ilmenite while allowing the throughflow of gas to fluidize the bed. During activation, the temperature was kept between 930 and 970 °C. Each redox cycle was initiated by fully oxidizing the ilmenite with five percent O_2 in N_2. Oxidation was followed by a flush of N_2 before the reduction with syngas (50% CO and 50% H_2) for rock ilmenite and methane for synthesized ilmenite. Before the initiation of the next cycle, the reactor was once again flushed with N_2 to avoid mixing fuel and air. The cycles were repeated until stable reactivity was achieved. The activated samples are referred to as OC1b and OC2b. The procedure and laboratory equipment[34] have been applied previously to evaluate and activate oxygen carriers.[35]

3. METHODS

3.1. Analytical Methods. The composition of synthetic ilmenite was analyzed using inductively coupled plasma-optical emission spectrometry (ICP-OES) spectrophotometer Xpectroblue-EOP-TI FMT26, a method suitable for detecting elements down to 0.1 wt %. The solid samples were prepared by a borate fusion process. The same procedure was used to determine the zinc concentration in sample OC3, before and after experiments.

3.1.1. Brunauer−Emmett−Teller (BET) Specific Surface Area. The specific surface area of the particles was examined by N_2 adsorption−desorption isotherms with Micrometrics ASAP 2020 surface area and porosity analyzer operating with liquid nitrogen. The resulting data were evaluated by Brunauer−Emmett−Teller (BET) theory to generate a specific surface area. Prior to the analysis, the samples were degassed under a flow of nitrogen for 4 h at 110 °C.

3.1.2. Phase Characterization. Crystalline phases of samples before (calcined and activated) and after experiments with the zinc compounds, were analyzed by X-ray diffractometry (XRD). The phase analysis was performed using a PANalytical Empyrean diffractometer with Cu Kα radiation (λ = 1.5406 Å) operating at 40 kV and 40 mA. Scans were made over a 2θ range of 5−90° with a step size of 0.008°. The detection limit for this technique is a few weight percent and thus not suitable to detect phases with low concentrations. Furthermore, if the sample contains amorphous specimens, low concentration phases could become difficult to identify. Therefore, complementing characterization techniques and thermodynamic equilibrium calculations were utilized in this work.

3.1.3. Morphology and Chemical Distribution. The morphology of the particles and the cross-section was examined using scanning electron microscopy (SEM) coupled with energy-dispersive X-ray spectroscopy (EDX). The system used for this investigation was Prisma ESEM from Thermo Scientific. The elemental distribution was examined using point analyses, line scans, and elemental mappings. Surface morphology and elemental composition were studied by mounting the particles on carbon tape. Particle cross section was studied by molding particles in epoxy resin. Samples were thereafter polished to expose the interior of the particles, and hence be able to study the interaction and penetration depth in detail. As the surface of the sample prepared in epoxy is nonconductive, the samples were sputter coated with a 5−6 nm thin layer of silver. Investigations were performed in high vacuum, at an accelerating voltage of 20 kV.

To make sure that a representative particle is analyzed, the samples were studied stepwise, and the following procedure was followed. First, chemical mappings of a multitude of particles were analyzed concerning the chemical distribution of zinc across the sample. Magnification was thereafter increased and a selection of particles representing the sample was further studied by chemical mapping, point analyses, and line scans. The outer layer was investigated in more detail using a depth profile.

3.2. Zinc Saturation Fraction (SF). To indicate the level of zinc interaction with ilmenite, spectra from the chemical maps of the cross-section analyses were used for element quantification. The zinc saturation fraction (SF) was used to evaluate the chemical maps and quantify the fraction of zinc in ilmenite, by relating zinc to the iron content in ilmenite. The spinel $ZnFe_2O_4$ is deemed the most stable zinc-bearing phase according to thermodynamic calculations, see Section 3.4.1, and it has also been observed in previous studies with ilmenite.[14,15,20] The saturation fraction indicates how close zinc is to saturating all available iron in ilmenite. In the case of used ilmenite, SF relates zinc to solely ilmenite particles. This is necessary as the used ilmenite also contains impurities in the form of silica sand particles, as well as other species that may bind Zn. Of course, a significant fraction of iron will be in the form of hematite, pseudobrookite, or ilmenite but the saturation fraction will provide a value for the maximum possible uptake of zinc in the form of $ZnFe_2O_4$ in the oxygen carrier. The maximum amount of zinc in the spinel phase is the iron concentration divided by two.

https://doi.org/10.1021/acs.energyfuels.3c01052
Energy Fuels 2023, 37, 7856−7870

$$\text{saturation fraction [\%]} = \frac{\text{Zn concentration}}{\text{maximum Zn uptake as Zn } Fe_2O_4} = \frac{Zn_{\text{atomic concentration}}}{Fe_{\text{atomic concentration}}/2}$$

3.3. Thermodynamic Equilibrium Calculations. To understand the influence on the phase stability during the addition of zinc, equilibrium calculations were performed using FactSage 8.2[36] with the databases FactPS, FToxid, FTsalt, and HSCA. The input to the calculations is based on the composition defined in Table 2. The results illustrate the evolution of phases during the addition of zinc. The calculation included 40 gaseous species, 78 stoichiometric solids, 120 solution species, and 18 solid solutions. Selected solid solutions were SlagA, SpinC, MeO_a, cPyrA, WOLLA, bC2SA, aBC2SB, Mel_A, OlivA, Mull, CAFS, CAF6, CAF3−1, C2AF, C3AF, CORU, ZNIT, WILL, Neph, Feld, TiO2, ILMEA, PSEU, TiSp, CaTi, PERO, KASH, KA_H, KA_L, bbAl, b_Al from FToxid, and SaltF, B4 (wurtzite) and hP22 (K_2SO_4) from FTsalt. Furthermore, the composition over an ash layer, as obtained from the depth profile, was studied using the same solid solutions. All identified species in the depth profile, excluding carbon, were used as input, and an inert atmosphere was set by fixing the activity of N_2 to 0.999.

Table 2. Composition of the Ilmenite Oxygen Carriers[a]

oxygen carrier element [wt %]	synthesized ilmenite (OC1a)	rock ilmenite (OC2a)	used ilmenite (OC3)
Fe	35.1	33.3	19.0
Ti	27	23.9	16.0
Ca	0.05	0.3	10.8
Si		0.9	4.8
Mg		1.8	2.0
Al		0.3	1.5
Na		0.1	1.0
K		0.1	1.8
Zn		0.01	1.0

[a]Composition of rock ilmenite as obtained from the supplier. The synthesized and used ilmenite were obtained by ICP-OES and ICP-SFMS, respectively.

3.4. Experimental Setup. The experiments with zinc compounds and ilmenite oxygen carriers were performed in a vertical reactor setup consisting of a fixed-bed quartz reactor, enclosed in an electrically heated furnace. Downstream of the reactor, filters were installed to remove particles entrained in the off-gas, which was followed by heated gas lines, and a gas analyzer schematically illustrated in Figure 2. The electrically heated furnace consists of three heating zones and the maximum operating temperature is 1100 °C. The reactor is made of quartz, with an outer/inner diameter of 12/10 mm, respectively, and a total length of 900 mm. Metallic zinc experiments were performed using a nitrogen flow of 200 mL/min as carrier gas. For zinc chloride experiments, the nitrogen flow passed a bottle filled with deionized water creating a flow with ∼2 vol % H_2O. The steam concentration was confirmed by the gas analyzer in an experiment with an empty reactor. The reactor was divided into two stages using silica wool. The wool was used to support the alumina crucible and the oxygen carrier while allowing the throughflow of gas. Common for both experiments, with $ZnCl_2$ and Zn, is that the system was heated in a nitrogen atmosphere and samples were left to cool inside the reactor in a nitrogen atmosphere before being collected and analyzed. Experiments were conducted for 60 min to ensure complete devolatilization of zinc compounds. The crucible was weighed before and after the experiments. The produced gases pass heated filters and gas lines before reaching the Fourier transform infrared (FTIR) spectrometer of type Gasmet DX-4000, with sampling cell and lines heated to 180 °C to avoid condensation. The spectrometer monitored the concentrations of H_2O, HCl, and SO_2. A background calibration was done using nitrogen before each experiment. Data were collected during experiments with a sampling frequency of 10 scans/min.

The three heating zones allow control of the partial pressure of the zinc compounds. The temperature at the position where metallic Zn and $ZnCl_2$ were located, were 715 and 640 °C, corresponding to partial pressures of 0.1 and 0.21 atm of Zn and $ZnCl_2$, respectively. The temperature for the position of the ilmenite was 900 °C for

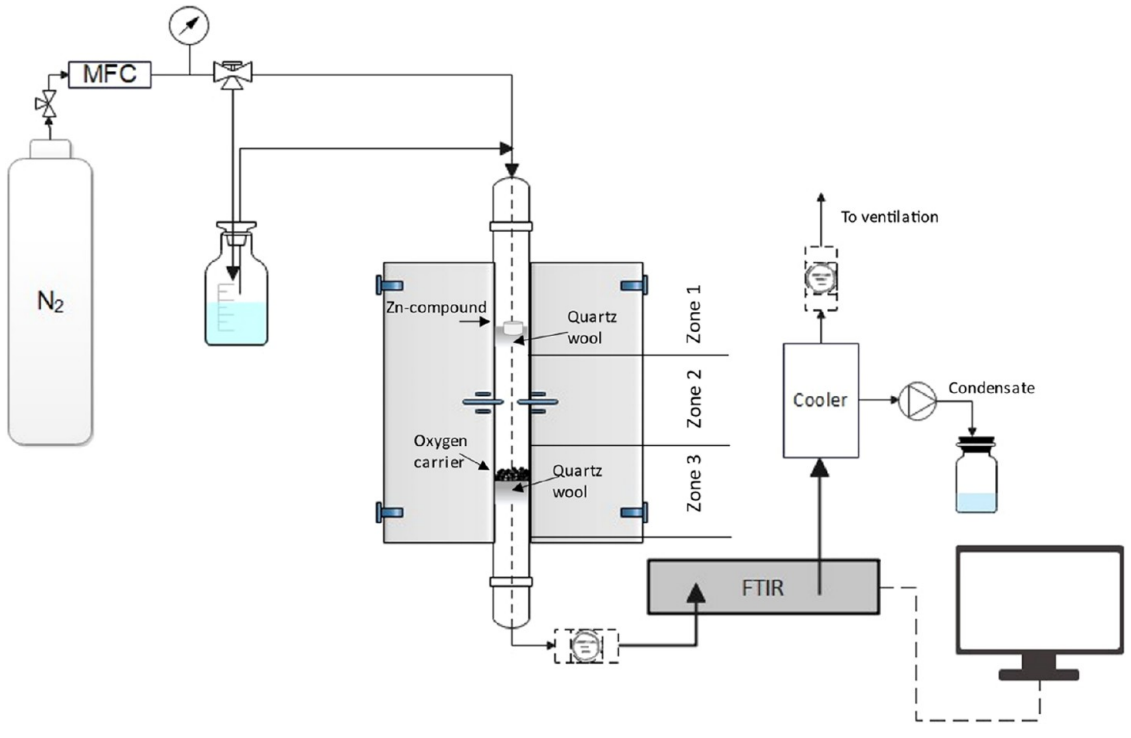

Figure 2. Schematic view of the experimental setup used for investigating the interaction between gaseous zinc compounds and oxygen carriers.

https://doi.org/10.1021/acs.energyfuels.3c01052
Energy Fuels 2023, 37, 7856−7870

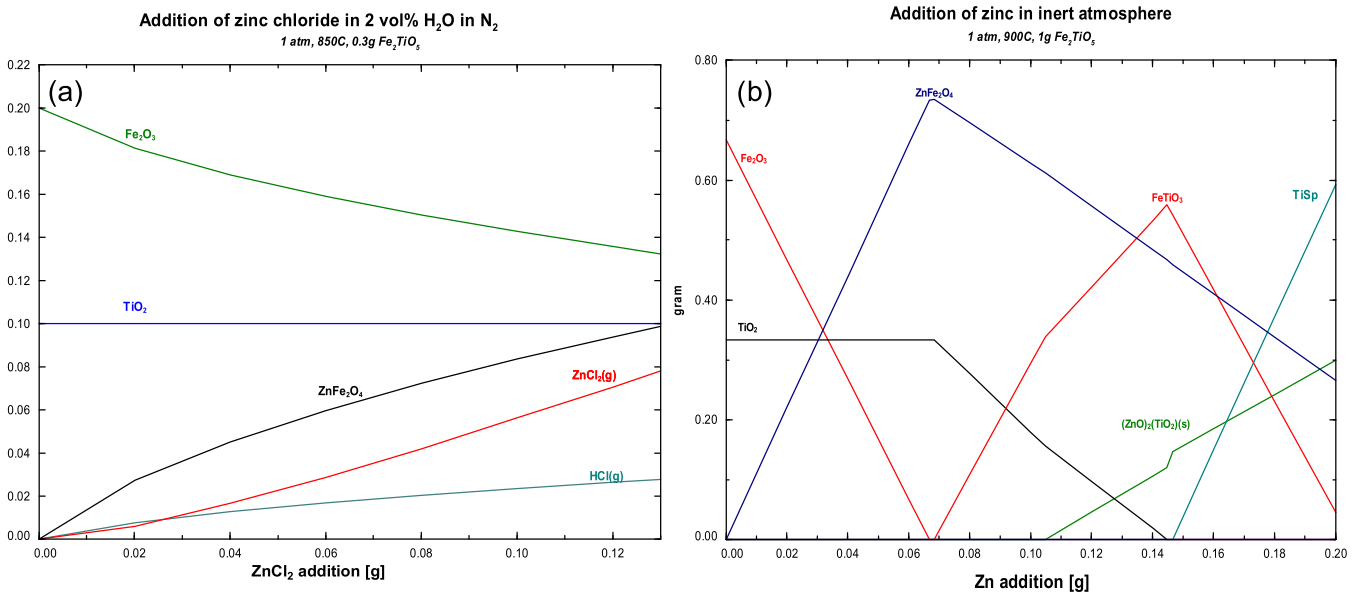

Figure 3. (a) Evolution of phases during experiments with zinc chloride. Addition of 0.13 g of zinc chloride to 0.3 g of oxidized ilmenite (Fe_2O_3 + TiO_2) at 1 atm, 850 °C, and 2 vol % H_2O. (b) Evolution of phases during experiments with metallic zinc. Addition of 0.2 g of zinc to 1 g of oxidized ilmenite (Fe_2O_3 + TiO_2) at 1 atm and 900 °C.

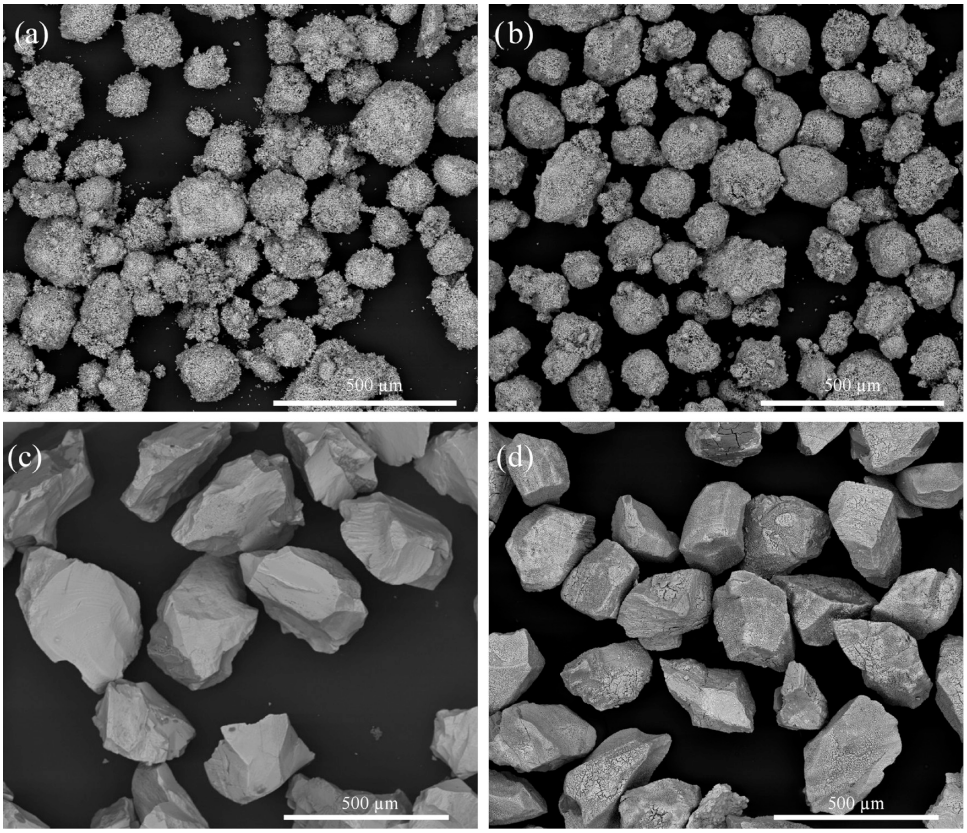

Figure 4. (a) Surface micrographs of synthesized ilmenite (OC1a), (b) activated synthesized ilmenite (OC1b), (c) rock ilmenite (OC2a), and (d) activated rock ilmenite (OC2b).

metallic zinc experiments and 850 °C for $ZnCl_2$ experiments, as these are average temperatures in an FR during CLC and OCAC, respectively. The positions for the alumina crucible and oxygen carrier were determined by the temperature profile measured beforehand, shown in Figure S5 in the Supporting Information (SI). The crucible containing the zinc compounds was located 340 mm upstream of the ilmenite. The zinc to ilmenite weight ratio was 0.2:1 in both experiments. At the top stage of the reactor, the alumina crucible was placed holding 0.2 g of Zn powder or 0.13 g of $ZnCl_2$, and at the bottom stage 1.0 or 0.3 g of oxygen carrier, respectively. Different weights were used due to the volume limitation of the alumina crucible. The gaseous zinc compounds were carried by the gas to the bottom stage and through the oxygen carrier bed. The remains in the alumina crucible were on average 5.2 and 4.1 wt % for

https://doi.org/10.1021/acs.energyfuels.3c01052
Energy Fuels 2023, 37, 7856−7870

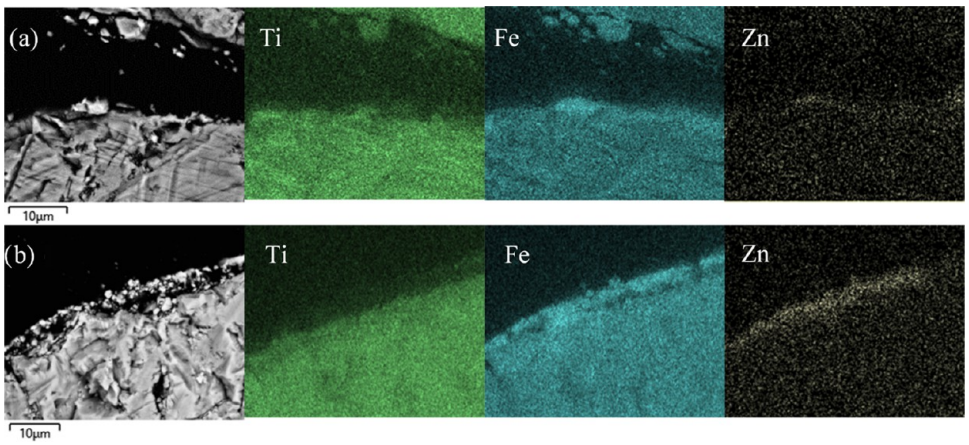

Figure 5. Cross-section micrographs of rock ilmenite (a) after experiments with $ZnCl_2$ and activated rock ilmenite (b) along with chemical maps of titanium, iron, and zinc.

the $ZnCl_2$ and Zn powder experiments, respectively, and attributed to the impurities of the zinc compounds.

3.4.1. Gaseous Conditions. Thermodynamic calculations performed before the start of this study suggested that experiments with zinc chloride in an inert atmosphere would not interact with the oxygen carrier, as shown in Figure S4 in the SI, while a few percent steam would enhance the interaction as seen in Figure 3a. The first experiments were thus conducted with zinc chloride and rock ilmenite in an inert atmosphere without steam. After experiments, the oxygen carrier was investigated by scanning electron microscopy coupled with energy-dispersive X-ray spectroscopy (SEM–EDX), but no zinc could be observed in the sample. The evolution of phases during the addition of zinc chloride is shown in Figure 3b, and according to these results, the expected compounds after experiments with $ZnCl_2$ in steam are $ZnFe_2O_4$, Fe_2O_3, and TiO_2.

The effect of steam on metallic zinc was also investigated experimentally by introducing 2 vol % steam with synthesized ilmenite. The steam oxidized zinc in the alumina crucible, which had increased in weight after the experiment, and prevented evaporation. Consequently, no interaction was observed with the oxygen carrier. It is however worth noticing that the gaseous conditions in the FR during CLC could contain both metallic zinc and steam, if the reduction potential is high enough.[15] The evolution of phases during the addition of metallic zinc to an ilmenite system is presented in Figure 3b. The expected phases after the addition of 0.2 g of Zn are $FeTiO_3$, $ZnFe_2O_4$, titania spinel ($FeTi_2O_4$), and $(ZnO)_2(TiO_2)$.

4. RESULTS AND DISCUSSION

4.1. Oxygen Carrier Composition. The elemental composition of the three oxygen carriers is presented in Table 2. It is observed that synthetic ilmenite (OC1a) contains the least amount of impurities. Rock ilmenite (OC2a) has a slightly higher iron content in comparison, but also some magnesium, silicon, and some other impurities. The used ilmenite also contains ash elements, such as calcium, silicon, sulfur, alkali, etc. Used ilmenite (OC3) is the most heterogeneous sample but based on the particle size, the concentration of ash compounds in the particles, and the morphology it is possible to compare particles based on their residence time. Fresh ilmenite particles have had less time to interact with the ash compounds which is why for example, the calcium concentration in the particles is low. With increased exposure time, particles are covered with a calcium layer that migrates toward the ilmenite core. Therefore, particles covered in calcium are considered to have been exposed to ash for a longer period.

4.2. Ilmenite Activation. The morphology of samples OC1 and OC2 were investigated by SEM–EDX. Micrographs of the particle surfaces before and after activation are shown in Figure 4. There were no visible structural changes between sample OC1a and OC1b although the diffractogram of the activated sample (OC1b) indicated a slight phase separation of iron and titanium, see for example Figure S1 in the Supporting Information. Sample OC2b showed the formation of cracks and a small iron-rich layer present on the particle surface, the iron-rich layer is shown in Figure S7 in the SI. The cracks are visible in the micrographs presented in Figures 4 and S6. An increased content of hematite (Fe_2O_3) was also observed in the diffractogram for the activated rock ilmenite, shown in Figure S2 in the SI. It is observed in Figure 4 that the porosity of synthesized ilmenite is higher in contrast to rock ilmenite. This is also reflected in the BET surface area, presented in Table 1. The table also shows an increase in the surface area after activation of the oxygen carrier.

4.3. Interaction between Oxygen Carriers and Zinc Chloride. After experiments with metallic zinc and zinc chloride, the ilmenite samples were analyzed concerning morphology, chemical distribution, composition, and crystalline phases. Thermodynamic calculations were then performed and related to the observations for further understanding of the interactions between ilmenite and zinc.

4.3.1. Synthesized Ilmenite. The crystalline phases of synthesized ilmenite (OC1a) were pseudobrookite and rutile with a trace amount of hematite, shown in Figure S1 in the Supporting Information (SI). There was a subtle difference in crystalline phases for synthesized ilmenite before and after activation showing a slight increase in hematite (Fe_2O_3), shown in Figure S1 in the SI. It is therefore not surprising that the experiments with samples OC1a and OC1b showed similar results. Chemical maps of the surface of samples OC1a and OC1b following exposure to $ZnCl_2$ at 850 °C did not show accumulation of zinc, although some zinc chlorides were found on a few particles. The surface micrograph and corresponding chemical maps are shown in Figure S8 in the SI. Since $ZnCl_2$ is gaseous at experimental temperatures the observation of chlorides is likely a result of handling the sample during the extraction of the material from the reactor and is not attributed to chemical reactions at high temperatures. Point analyses and line scans performed over the particle cross-sections confirmed

https://doi.org/10.1021/acs.energyfuels.3c01052
Energy Fuels 2023, 37, 7856–7870

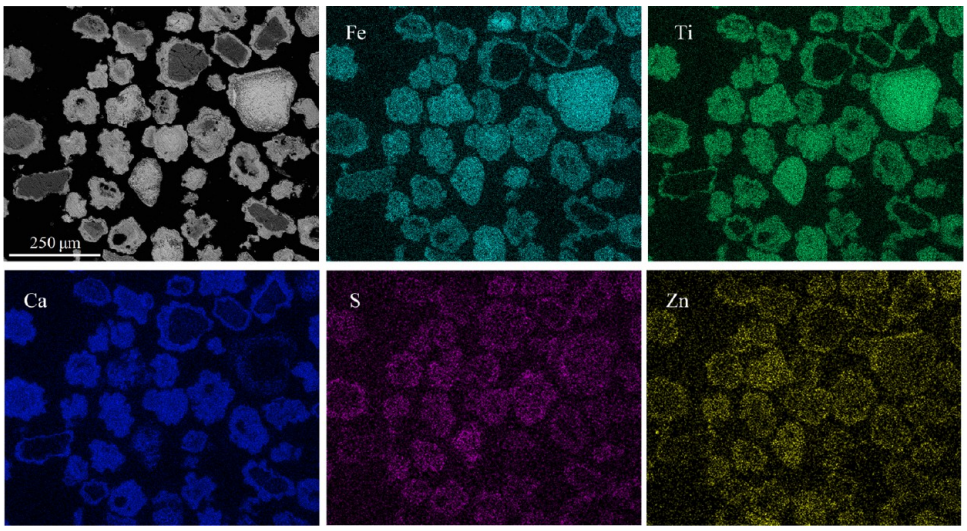

Figure 6. Micrograph of the cross section of used ilmenite (OC3) after experiments with $ZnCl_2$. Chemical mappings of iron, titanium, calcium, sulfur, and zinc are presented.

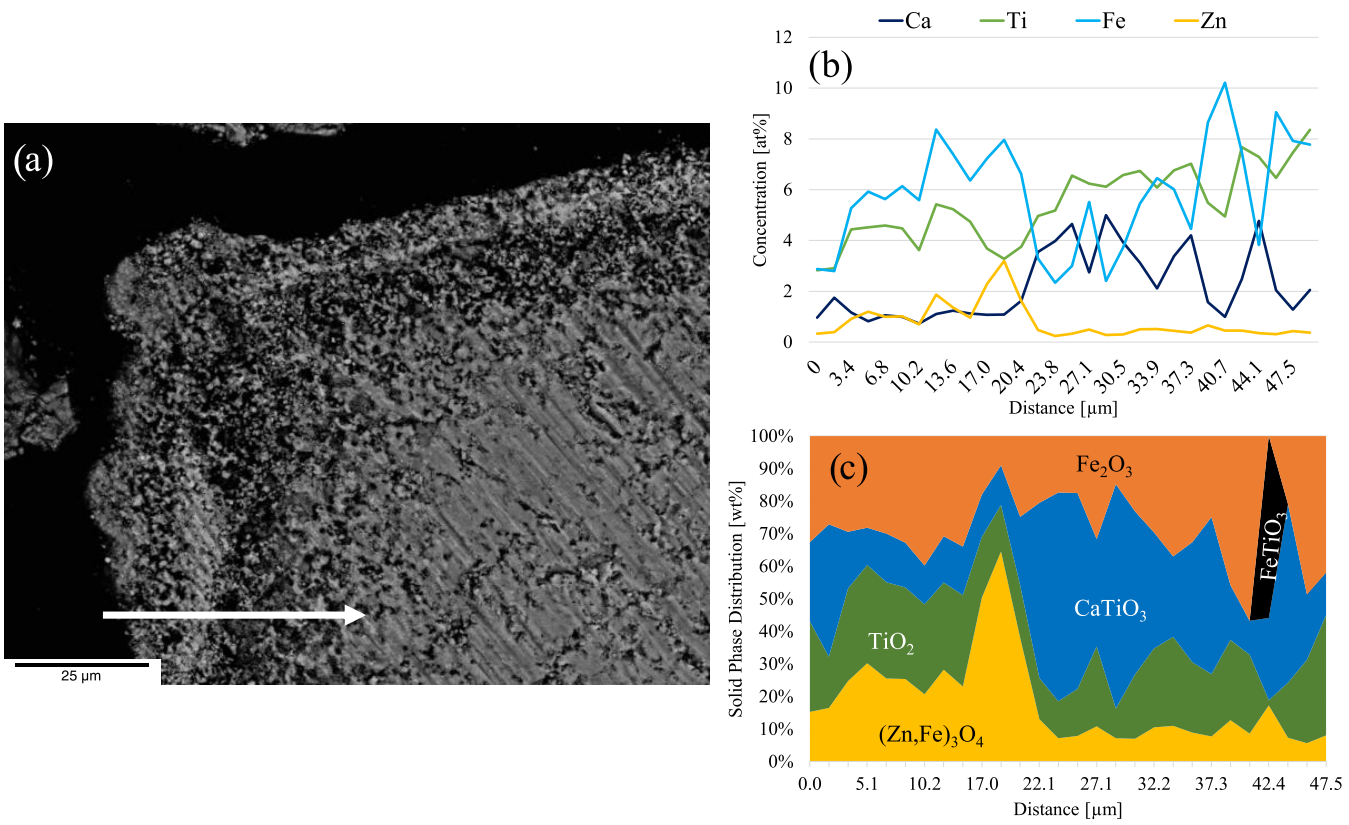

Figure 7. (a) Micrograph of the cross section of used ilmenite (sample OC3) after experiments with zinc chloride. The depth profile was performed along the white arrow, (b) depth profile over the ash layer, and (c) solid-phase distribution across the line scan according to thermodynamic calculations, performed in an inert atmosphere at 850°C and 1 atm.

that there was no interaction between zinc chloride and synthesized ilmenite.

4.3.2. Rock Ilmenite. Micrographs and chemical maps of the cross section of ilmenite samples (OC2a and OC2b) after experiments with $ZnCl_2$ are presented in Figure 5. For sample O2a, there were only small areas of the particle surface where the zinc and iron concentrations were enhanced. Activated ilmenite, on the other hand, showed a zinc layer on the surface of the particle, see Figure 5b. Point analyses and line scans showed that the chlorine concentration was negligible, which points toward the partitioning of chlorine to the gas phase. HCl was observed by the gas analyzer during the experiments. The results indicate that the iron-rich layer formed during the activation of ilmenite enhances the interaction with $ZnCl_2$. The saturation fraction (SF) is used to evaluate the chemical maps and the level of interaction. The saturation fraction in Figure 5 is 1% before, and 3% after the activation of the sample. In

https://doi.org/10.1021/acs.energyfuels.3c01052
Energy Fuels 2023, 37, 7856−7870

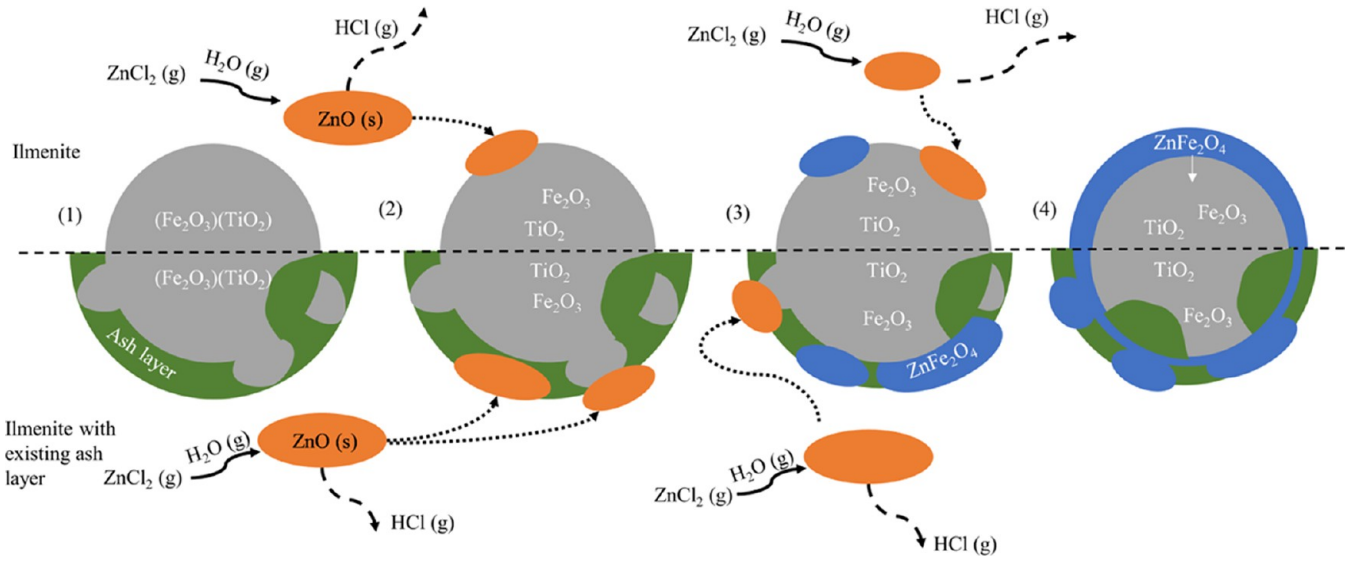

Figure 8. Illustration of the mechanism behind the interaction between zinc chloride and ilmenite in steam and N_2, at 850 °C and 1 atm. The top illustrates the mechanism for ilmenite, and the bottom half shows the mechanism for ilmenite with an existing ash layer.

general, more interaction was seen between $ZnCl_2$ and rock ilmenite samples than between $ZnCl_2$ and synthesized ilmenite.

4.3.3. Used Ilmenite. Sample OC3 consists of rock ilmenite extracted from the bottom bed after 200 h of OCAC operation with recycled waste wood and wood chips. The sample, therefore, contains ash-forming elements such as calcium, potassium, and sulfur, as seen in Table 2. For the same material, previous studies report the surface zinc concentration to be 0.5−1.5 atom %.[20] Chemical maps of the cross section before the experiments are presented in Figure S9 in the SI for reference. The used ilmenite contains zinc, which is present both in the outer ash layer and across the particle cross section.

Point analyses on the particle surfaces after experiments with $ZnCl_2$ reveal zinc concentrations between 3 and 9 atom %. The chemical maps of the cross section and surface of used ilmenite after experiments with $ZnCl_2$ are presented in Figures 6, S10, and S11 in the SI. In contrast to Figure S9 in the SI, the intensity of zinc surrounding the particles has increased. Figure 6 shows that zinc is found in combination with high iron concentrations and ilmenite particles which are not completely covered with ash elements, represented by the major ash element calcium in the figure. The saturation fraction in Figure 6 is 34% which is higher than before the experiments (9.5%) pointing toward an accumulation of zinc. The zinc concentration in sample OC3, measured by ICP-OES, increased from 1.0 to 2.6 wt % after experiments.

A depth profile over the ash layer is presented in Figure 7. Figure 7b shows the concentration of zinc in the outer ash layer and its correlation with iron. The chemical maps of Figure 7a are shown in Figure S11 in the SI, where the saturation fraction is 19%. Both the line scan and chemical maps show that zinc accumulates in the inner ash layer along with iron. The enrichment of zinc in the iron-rich layer surrounding calcium has also been observed in OCAC operations with other fuels.[37] Figure 7b shows that a small amount of sulfur is present deeper into the particle, which correlates with calcium see Figure S11 in the SI, while sulfur on the outer surface correlates with potassium. Thermodynamic calculations were performed at each point of the line scan using the concentrations of Fe, Ti, Zn, Ca, S, and O as input. The stable solid phases in each point are presented in Figure 7c. The only zinc-bearing compound is shown to be spinel $(Zn,Fe)_3O_4$, with the major constituent being $ZnFe_2O_4$, which is accumulated in the outer layer.

4.4. Mechanism for $ZnCl_2$. The results in this study indicate that the reaction between zinc chlorides and ilmenite is low but that the presence of steam can promote the interaction. The first experiments were thus conducted with zinc chloride and rock ilmenite in an inert atmosphere without steam. After experiments, the oxygen carrier was investigated by SEM−EDX, but no zinc could be observed in the sample. Jones et al. studied the thermal stability of zinc compounds in air and found that $ZnCl_2$ vaporizes above 400 °C and partly oxidizes to ZnO.[38] ZnO has a melting temperature above 1900 °C and is thus stable at high temperatures. Considering that no interaction was observed with ilmenite in a nitrogen environment, it is most likely that steam first promotes oxidation to ZnO which in its turn interacts with the oxygen carrier. This is further supported by the observed HCl in the gas phase.

The interaction between ilmenite and $ZnCl_2$ in N_2 and steam is illustrated in Figure 8. First, the oxidation of zinc chloride to zinc oxide and HCl occurs in the gas phase (1). When ZnO comes in contact with the iron-rich layer (2) it forms $ZnFe_2O_4$ (3) as observed in Figure 6. With continuous exposure to $ZnCl_2$ in steam, ZnO (3) forms along with continuous release of HCl (g). Furthermore, this interaction is enhanced after the activation of ilmenite due to the formation of an iron-rich layer. This also explains why there was limited interaction between synthesized ilmenite and zinc chloride. With time (4), the zinc ferrite layer grows until the surface has been saturated with Zn. If the sample were to be treated in consecutive cycles of reduction and oxidation a deeper zinc ferrite layer could form due to the migration of iron toward the surface leading to a Fe_2O_3 layer above the Zn-layer. A similar mechanism is observed when there is an ash layer, and the main difference with an ash layer is that the ash could restrict contact with iron which can prevent or slow down the interaction. Like the case with no ash, a zinc ferrite layer is observed but also located beneath the ash layer.

https://doi.org/10.1021/acs.energyfuels.3c01052
Energy Fuels 2023, 37, 7856−7870

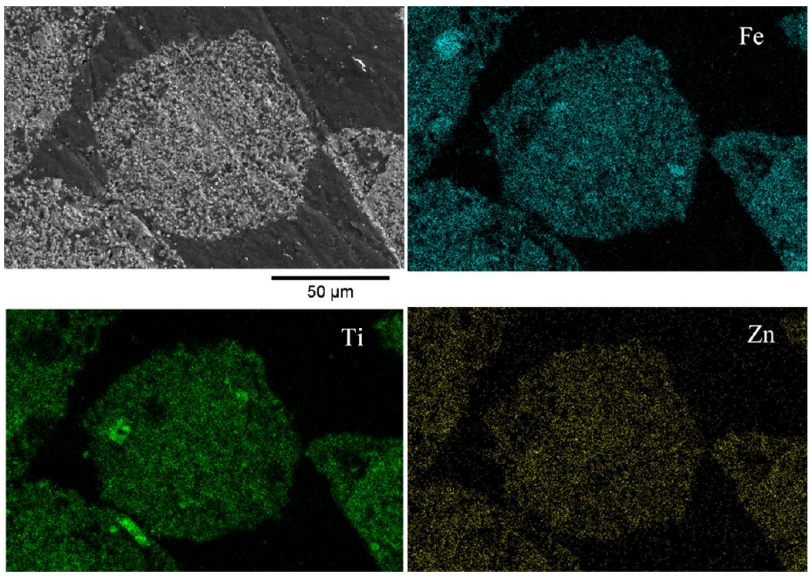

Figure 9. Micrograph of the cross section of synthesized ilmenite (OC1a) after experiments with metallic zinc along with chemical maps of iron, titanium, and zinc.

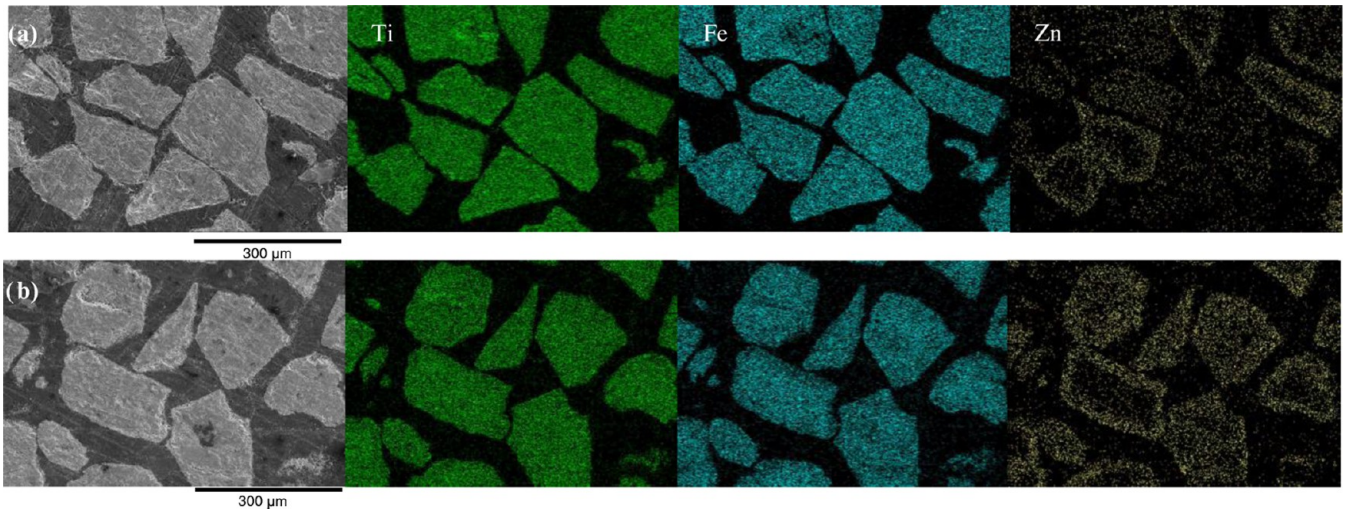

Figure 10. Cross-section micrographs of ilmenite after experiments with metallic zinc (sample OC2a, a) and activated ilmenite (sample OC2b, b) along with the elemental maps of titanium, iron, and zinc.

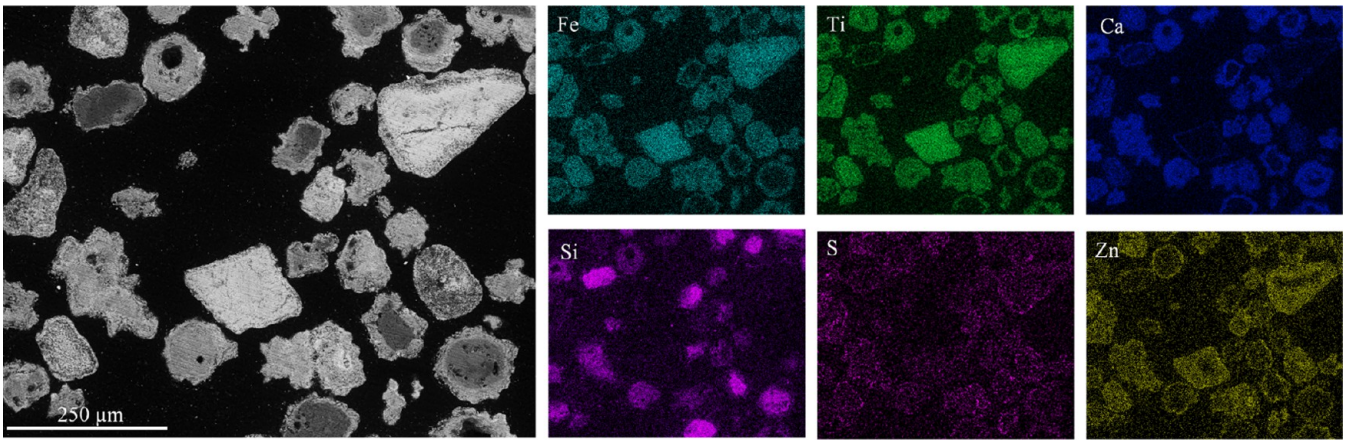

Figure 11. Cross-section micrograph of used ilmenite after experiments with zinc (sample OC3) and the corresponding chemical maps of iron and titanium along with the elements calcium, silicon, sulfur, and zinc.

https://doi.org/10.1021/acs.energyfuels.3c01052
Energy Fuels 2023, 37, 7856−7870

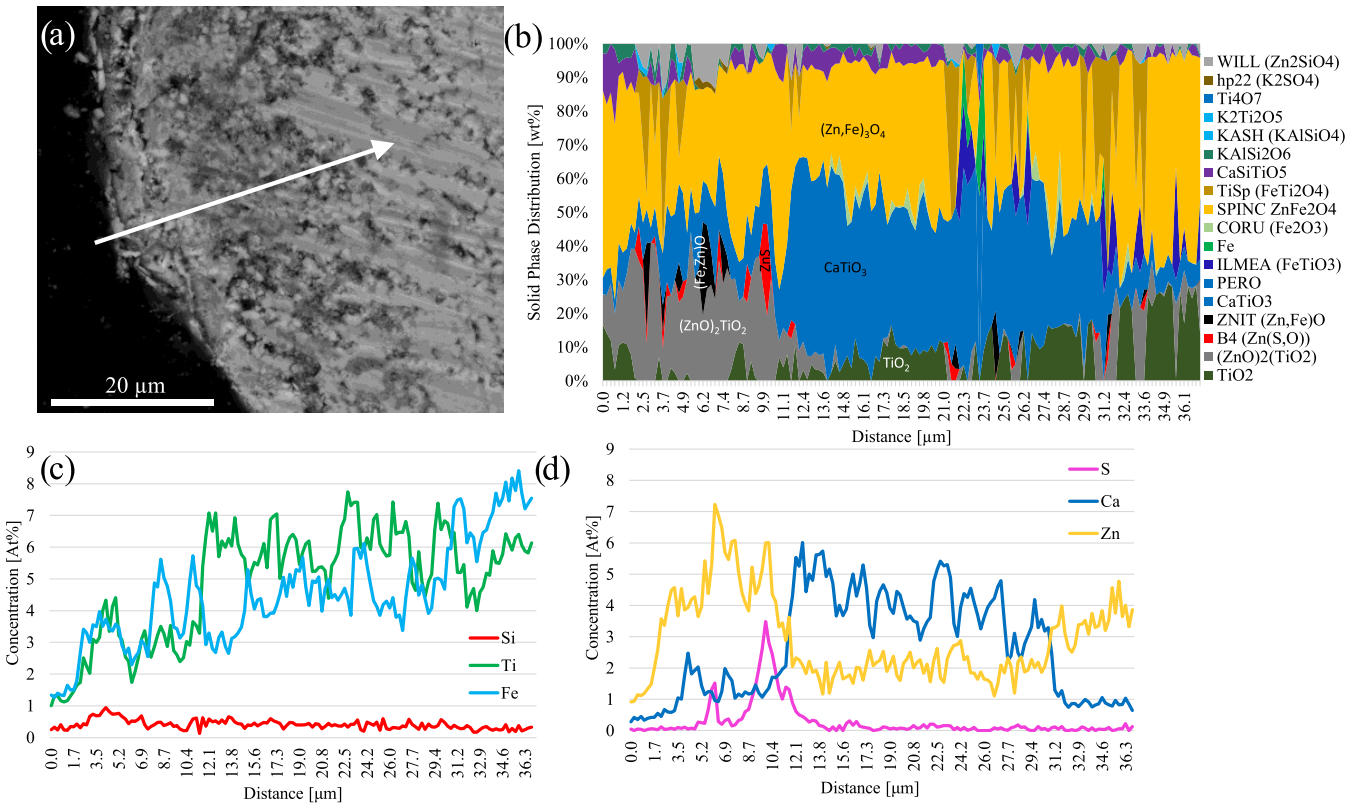

Figure 12. (a) Micrograph of the ash layer of used ilmenite (OC3) after experiments with metallic zinc. Line scan performed along the white arrow. (b) Solid phases according to thermodynamic calculations at 900 °C and 1 atm. The major phases and zinc-bearing phases are indicated in the figure. The complete list is provided in the legend. The line scan over the ash layer shows Fe, Ti, and Si in (c) and Ca, Zn, and S in (d).

4.5. Interaction between Oxygen Carrier and Metallic Zinc. *4.5.1. Synthesized Ilmenite.* The elemental maps for synthesized ilmenite after experiments with metallic zinc, showed an even zinc distribution across the particle cross section, see Figure 9. The saturation fraction for sample OC1a was 79%. The observations after zinc experiments were similar before and after the activation of the synthesized ilmenite. In contrast to experiments with zinc chloride, deeper penetration was observed when synthesized ilmenite was exposed to metallic zinc as it covered the particle cross section completely. The high surface area of the synthesized ilmenite, as opposed to rock ilmenite, is likely the reason for the prominent interaction with metallic zinc. The saturation fraction was 79% for synthesized ilmenite and 53% for activated rock ilmenite, shown in Figure 10. The synthesized ilmenite was reduced after experiments, from pseudobrookite (Fe_2TiO_5) to ilmenite ($FeTiO_3$) and spinel ($ZnFe_2O_4$). Some zincite (ZnO) was also observed in the diffractogram.

4.5.2. Rock Ilmenite. Micrographs and elemental maps of the cross section of OC2a and OC2b after experiments with metallic zinc are presented in Figure 10. The elemental maps showed a clear interaction between rock ilmenite and zinc. From Figure 10, it is also clear that the activated ilmenite accumulates more zinc. The crack formation after activation will facilitate the transportation of zinc through the particles. The interaction was also more prominent for Zn as opposed to $ZnCl_2$. This is reflected in the saturation fraction in Figure 10, which is 23% before and 53% after the activation. The crystalline phases after experiments with metallic zinc, presented in Figure S2 in the SI, were shown to be ilmenite ($FeTiO_3$), spinel ($ZnFe_2O_4$), and some zincite (ZnO).

4.5.3. Used Ilmenite. Studying the chemical distribution of zinc in sample OC3 after experiments with metallic zinc, see Figure 11, shows zinc in combination with iron as expected. In contrast to experiments with zinc chloride, the particles seemed to be covered in zinc, even those which were covered in calcium. The depth of interaction was more prominent in ilmenite particles with thinner ash layers. The saturation fraction in Figure 11 is 120%, meaning that the spinel phase could not possibly be the only zinc-bearing phase. The diffractogram, shown in Figure S3 in the SI, showed a clear increase of the spinel ($ZnFe_2O_4$) phase along with the perovskite $CaTiO_3$ and minor amounts of wurtzite ZnS and zincite ZnO. The zinc concentration in sample OC3, measured by ICP-OES, increased from 1.0 wt % before, to 11.3 wt % after experiments.

A line scan and chemical maps over a particle with an ash layer, Figures 12 and S12, respectively, show a high zinc concentration in the outer layer of the particle. The saturation fraction in Figure 12 is 118%. Thermodynamic calculations were performed at each point of the line scan using the concentrations of Fe, Ti, Zn, Ca, K, Si, Al, S, and O as input. The phases in each point are presented in Figure 7b. Results showed that in the outer ash layer, 0.0−9.9 μm depth, there is likely a combination of $ZnFe_2O_4$ and $(ZnO)_2TiO_2$ with smaller amounts of ZnO and ZnS. The presence of ZnO, ZnS, and the inverse spinel $(ZnO)_2TiO_2$ explains why the saturation fraction in Figure 11 has a value above 100%. In the deeper ash layer, between 11.1 and 31.2 μm, see Figure 7b,c, there was a clear correlation between Ca−Ti and Zn−Fe, which according to thermodynamic calculations is the perovskite $CaTiO_3$ and spinel $ZnFe_2O_4$. The spinel ($ZnFe_2O_4$), perovskite ($CaTiO_3$),

https://doi.org/10.1021/acs.energyfuels.3c01052
Energy Fuels 2023, 37, 7856−7870

rutile (TiO_2), wurtzite (ZnS) and zincite (ZnO), and zincite (ZnO) were all observed in the diffractogram of sample OC3, see Figure S3 in the SI.

The surface of the particles from sample OC3 showed an interesting feature as they were covered with micrometer-sized crystals. A surface micrograph showing the area of interest is presented in Figure 13. A magnification of the micro-sized crystals along with chemical maps, presented in Figure S13 in the SI, shows the coexistence of zinc and sulfur in the crystals. Point analyses showed an equimolar Zn:S ratio and the diffractogram of the sample confirms the presence of wurtzite, ZnS, see discussion above. A recent study on ash interactions with ilmenite predicted the formation of ZnS in CLC with recycled waste wood.[15]

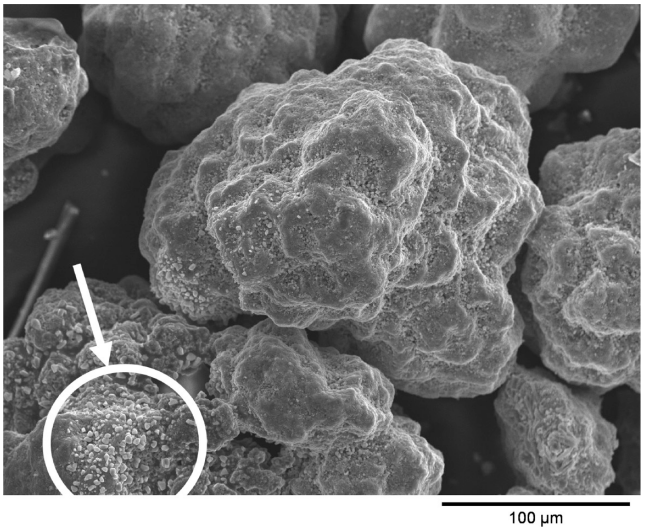

Figure 13. Surface micrograph of used ilmenite (OC3) after experiments with zinc. An area with micrometer-sized crystals appearing after experiments with zinc is pointed out in the figure.

During the experiments with metallic zinc and used ilmenite, the gas analyzer detected a release of SO_2 as the temperature increased above 850 °C. To better understand this phenomenon, the release of SO_2 was monitored during the heating of sample OC3 without zinc and with 0.1 g of zinc. In all cases, a release of SO_2 was observed, see the example in Figure 14. The gaseous conditions in the OCAC boiler, from which OC3 was obtained, were different from this study. In the boiler, the SO_2 partial pressure is higher and so switching to an inert atmosphere led to a release of SO_2. This is observed in the blank experiments in Figure 14.

Slightly higher SO_2 release was observed during experiments with zinc, see the example in Figure 14. The diffractogram of used ilmenite showed the presence of $CaSO_4$ but the temperature in the experiments in this work was not sufficiently high for the decomposition of calcium sulfate. However, it has been reported that the decomposition of $CaSO_4$ can occur at lower temperatures and especially if the conditions are reducing,[39] or in the presence of other metals, iron oxides for example.[40] During experiments with metallic zinc, the zinc gas will create a reducing atmosphere in the reactor and thereby favorable conditions for $CaSO_4$ decomposition. The diffractogram of sample OC3 showed that $CaSO_4$ decreases in intensity after experiments while ZnS appeared. Furthermore, alkali sulfates at the particle surface, seen in Figure S9 in the SI, could also contribute to the release of SO_2. Sulfur uptake during oxidizing conditions and the release during reduction has previously been established in ilmenite and attributed to the phases $CaSO_4$, K_2SO_4, and $K_2Ca_2(SO_4)_3$.[27]

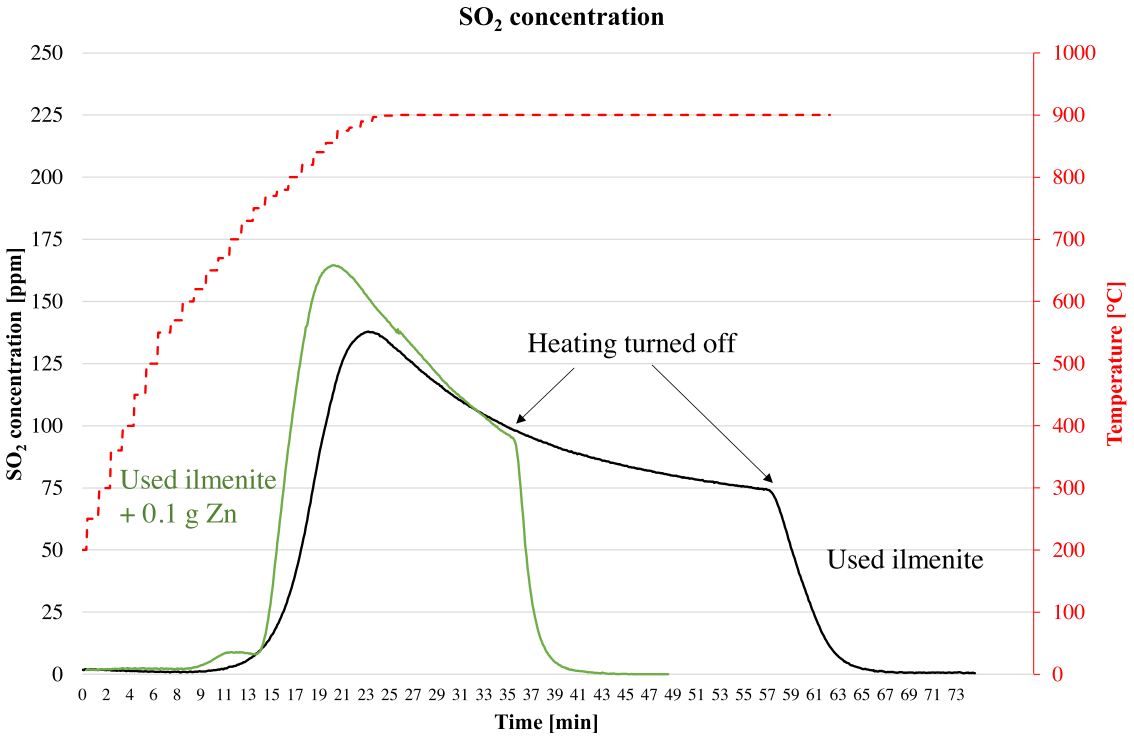

Figure 14. Examples of the SO_2-release detected by the gas analyzer during the blank run (black line) and experiments with used ilmenite and 0.1 g of zinc powder (green line). The reactor temperature at the position of ilmenite is shown on the secondary y-axis.

https://doi.org/10.1021/acs.energyfuels.3c01052
Energy Fuels 2023, 37, 7856−7870

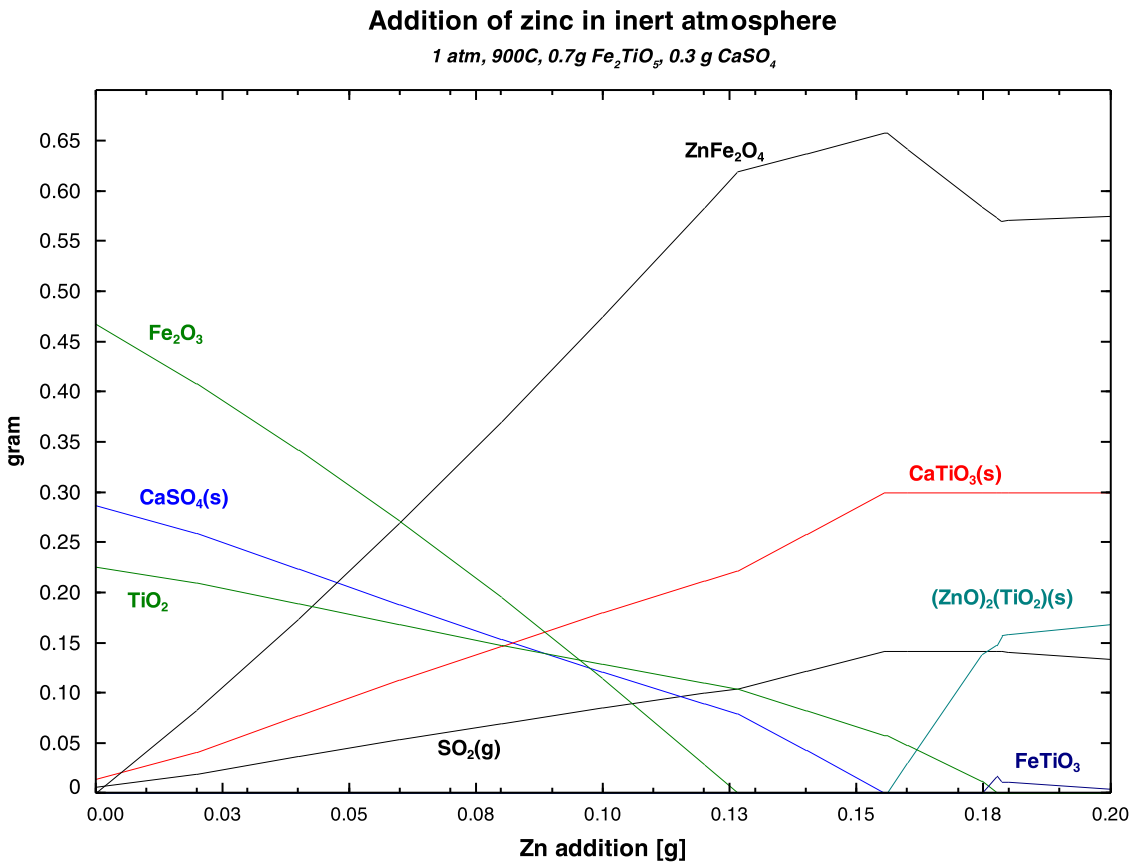

Figure 15. Results obtained from thermodynamic equilibrium calculations showing the evolution of phases during the addition of 0.2 g of zinc to 0.7 g of oxidized ilmenite (Fe_2O_3 + TiO_2) and 0.3 g of $CaSO_4$ (inert conditions, 1 atm, 900 °C).

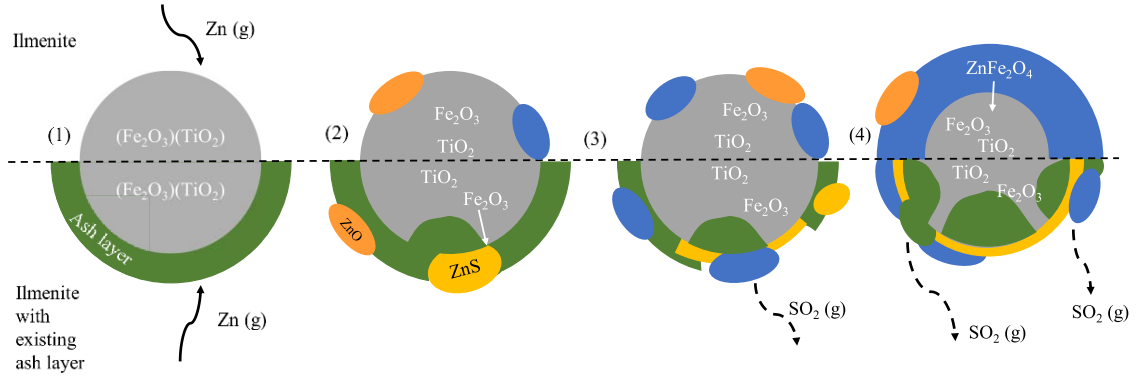

Figure 16. Illustration of the mechanism behind the interaction between zinc and ilmenite in an inert atmosphere, at 850 °C and 1 atm. The top illustrates the mechanism for ilmenite, and the bottom half shows ilmenite with an existing ash layer.

Zinc likely undergoes a series of reactions depending on the surface composition of the ilmenite particle and ash layer. The addition of Zn (g) to the gaseous phase surrounding an ilmenite system will lead to increased reduction potential and as previously mentioned, this will favor a release of SO_2. The release was further studied using thermodynamic calculations, and the system is defined based on the chemical composition obtained from SEM−EDX. Zinc was added stepwise to the system and the phase changes are reported in Figure 15.

The presence of ZnS is not predicted in Figure 15, indicating that the stability of other zinc-bearing compounds, such as $ZnFe_2O_4$, is higher. During the experiments, the elements Fe, Ti, Ca, and S were not equally accessible to Zn. For example, $CaSO_4$ is present on the outer surface of the OC3-particles and encounters the metallic gaseous zinc compound first. At these local conditions, ZnS is a stable compound and therefore observed experimentally in Figure 13. The phases reported in Figure 15 are based on the fact that all elements are equally available for reaction. It is expected that the experimental results consist of a combination of those in Figure 15 and local effects. As observed in Figure 15 the addition of Zn is accompanied by an immediate increase in $ZnFe_2O_4$ and $CaTiO_3$ along with a release of SO_2. $(ZnO)_2(TiO_2)$ is shown to be stable above 0.15 g of Zn addition which only forms after all Ca has reacted with TiO_2. The phase analysis showed that the major titanium phase was in the form of perovskite, $CaTiO_3$, while the major zinc-bearing phase was the spinel, $ZnFe_2O_4$, shown in Figure S3 in the SI. The spinel $ZnFe_2O_4$

https://doi.org/10.1021/acs.energyfuels.3c01052
Energy Fuels 2023, 37, 7856−7870

and inverse spinel $(ZnO)_2(TiO_2)$ were difficult to distinguish in the XRD diffractogram, but the wide peaks suggested that there could be a mixture present. Therefore, a combination of SEM−EDX and thermodynamic equilibrium calculations was used to provide insight into stable compounds. The evolution of phases for a pure ilmenite system is shown in Figure 3. Based on the thermodynamic calculations it is not unlikely that $(ZnO)_2(TiO_2)$ starts to form after zinc has interacted with all available iron. However, in chemical looping applications with solid fuels, the amount of calcium will always exceed those of zinc, which favors $CaTiO_3$ and thereby prevent $(ZnO)_2(TiO_2)$. Ultimately, in chemical looping applications, there will be a high driving force for the formation of zinc ferrites and calcium titanates.

4.6. Mechanism for Metallic Zinc. There are clear differences in the interaction pathways between ilmenite and zinc depending on the zinc compound and oxygen carrier properties. Comparing the outcome for the oxygen carriers between the two zinc compounds showed a higher saturation fraction in the case of metallic zinc. Observations from the characterization of the samples and thermodynamic equilibrium calculations were combined into an illustration, see Figure 16. The figure shows the proposed mechanism behind the interaction with Zn and ilmenite (top) and the influence of the ash layer (bottom). In the figure, metallic zinc is present in the gas phase (1). In the upper figure, contact between iron oxides and metallic zinc will result in ZnO and/or $ZnFe_2O_4$ (2). The reaction forming $ZnFe_2O_4$ is enhanced if ilmenite has been activated. Activation of ilmenite is known to increase the gaseous conversion of fuels,[32] but in this study, it is shown that activation also affects zinc chemistry. The iron-rich layer formed after the activation enhanced the interaction with both zinc and zinc chloride. After the activation of rock ilmenite, the saturation fraction increased from 0 to 3% for zinc chloride and from 23 to 53% for metallic zinc. The formation of cracks after activation facilitated the transportation of gaseous zinc compounds. So, the ilmenite reactivity toward zinc can be expected to increase with increasing residence time due to the iron migration to the surface and the formation of cracks. With continuous exposure to zinc, the zinc ferrite layer will grow (3) and with high concentrations of zinc, the formation of $(ZnO)_2(TiO_2)$ could also be viable. With time, a growing zinc ferrite layer is observed on the particle (4).

The mechanism explained above could also occur in ilmenite with an ash layer, where iron is accessible. However, an ash layer could also prevent direct contact between iron and Zn, see Figure 16(bottom). In such a case, Zn will first interact with $CaSO_4$ to form ZnS (shown in Figures 13 and S13) in combination with calcium titanate (Figure 15) (2). There is a subsequent reaction with iron oxides (3) with the products $ZnFe_2O_4$ and SO_2 (Figures 12 and S12−S14). With continuous exposure, the iron migration progresses and builds upon ZnS (3). With time, ash migrates inward, and the zinc ferrite layer grows on the particle (4) and is combined with a continuous SO_2 release. This results in a thick outer ash layer with zinc ferrites along with a ZnS layer, as shown in Figure S12, and supported by the crystalline phases observed in the diffractograms (Figure S3 in the SI).

4.7. Environmental Implications. The use of oxygen carriers during combustion of waste fuels could have environmental benefits, with lower emissions of gaseous impurities, and lower costs for carbon capture.[8,9] Hence, such chemical looping technologies could be instrumental in meeting climate targets.[10] The results from this study have environmental implications concerning the toxicity of ash streams from waste combustion and the possibilities for zinc recycling. Waste ashes from thermal treatment are contaminated with toxic elements but can also contain a considerable amount of valuable metals. Bottom ashes are commonly landfilled and extraction of valuable metals, such as zinc, is generally expensive and energy-consuming. It is shown here that utilizing ilmenite as a bed material will stabilize zinc in the form of zinc ferrites, a non-water-soluble compound.[41] Furthermore, the results show that interaction can be expected to be more prominent between metallic zinc and ilmenite, conditions encountered during CLC. Consequently, the fly ash could contain less zinc than that of OCAC and likely also normal fluidized bed combustion of waste. With lower heavy metal concentrations in the fly ash, the toxicity and handling could be facilitated. On the other hand, stabilization in ferrites in the bed material could be detrimental to Zn recycling procedures.

5. CONCLUSIONS

This study presents the first laboratory investigation of zinc with the oxygen carrier ilmenite, commonly utilized in CLC and OCAC. The zinc compounds investigated were metallic zinc and zinc chloride with three types of ilmenite; Norwegian rock ilmenite, synthesized ilmenite, and ilmenite extracted after 200 h of OCAC operation. The influence of activating rock ilmenite and synthesized ilmenite was also studied. After exposures in a two-staged vertical tube reactor, samples were analyzed concerning morphology and crystalline phases, and the observations were complemented with thermodynamic equilibrium calculations. The uptake of zinc in ilmenite samples was evaluated by the saturation fraction, which measures the maximum possible uptake of zinc in the form of $ZnFe_2O_4$. The interaction was observed to be influenced by:

- The type of zinc compounds. The interaction with metallic zinc was more prominent as opposed to zinc chloride.
    - After exposure with synthesized ilmenite, rock ilmenite, and used ilmenite the highest observed saturation fractions were 0, 3, and 34% with zinc chloride and 53, 79, and 120% for metallic zinc. The value above 100% indicates that other zinc-bearing phases, such as ZnS, could also be present.
- Activation of ilmenite.
    - The iron-rich layer formed after the activation of ilmenite enhances the interaction with both zinc and zinc chloride. After the activation of rock ilmenite, the saturation fraction increased from 0 to 3% for zinc chloride and from 23 to 53% for metallic zinc. The formation of cracks after activation facilitates the transportation of gaseous zinc compounds.
- The high porosity of synthesized ilmenite is likely the reason why it showed the highest degree of interaction with metallic zinc, where the highest observed saturation fraction was 79% in contrast to 53% of the activated rock ilmenite.
- The presence of an ash layer. Sulfates on the particle surface affect the reaction path as it allows ZnS to form on the surface with subsequent formation of zinc ferrites and calcium titanates and a release of SO_2. The

https://doi.org/10.1021/acs.energyfuels.3c01052
Energy Fuels 2023, 37, 7856−7870

saturation fraction increased from 9.5 to 34% after experiments with zinc chloride and to 120% after experiments with metallic zinc.

■ ASSOCIATED CONTENT

Supporting Information

The Supporting Information is available free of charge at https://pubs.acs.org/doi/10.1021/acs.energyfuels.3c01052.

Comparison of XRD patterns before and after experiments of synthesized ilmenite (Figure S1), rock ilmenite (Figure S2), and used ilmenite (Figure S3); evolution of phases during the zinc chloride to ilmenite without steam (Figure S4); temperature profile (Figure S5); surface micrograph of rock ilmenite before and after activation (Figure S6); chemical maps of sample OC2b (Figure S7); micrograph and chemical maps of sample OC1a after exposure with zinc chloride (Figure S8); and micrograph and chemical maps of used ilmenite before exposure (Figure S9), after exposure with zinc chloride (Figures S10 and S11), and after exposure with metallic zinc (Figures S12−S14) (PDF)

■ AUTHOR INFORMATION

Corresponding Author

Ivana Staničić − *Department of Space, Earth and Environment, Division of Energy Technology, Chalmers University of Technology, SE-412 96 Gothenburg, Sweden;* orcid.org/0000-0002-6927-4822; Email: stanicic@chalmers.se

Authors

Emil Ola Lidman Olsson − *CHEC Research Centre, Department of Chemical and Biochemical Engineering, Technical University of Denmark, 2800 Kongens Lyngby, Denmark; Sino-Danish College, University of Chinese Academy of Science, 101400 Beijing, China;* orcid.org/0000-0002-3544-9065

Hao Wu − *CHEC Research Centre, Department of Chemical and Biochemical Engineering, Technical University of Denmark, 2800 Kongens Lyngby, Denmark;* orcid.org/0000-0003-0462-2491

Peter Glarborg − *CHEC Research Centre, Department of Chemical and Biochemical Engineering, Technical University of Denmark, 2800 Kongens Lyngby, Denmark;* orcid.org/0000-0002-6856-852X

Iñaki Adánez-Rubio − *Instituto de Carboquímica (ICB-CSIC), 50018 Zaragoza, Spain*

Henrik Leion − *Chemistry and Chemical Engineering, Chalmers University of Technology, 412 93 Göteborg, Sweden;* orcid.org/0000-0002-9716-2553

Tobias Mattisson − *Department of Space, Earth and Environment, Division of Energy Technology, Chalmers University of Technology, SE-412 96 Gothenburg, Sweden;* orcid.org/0000-0003-3942-7434

Complete contact information is available at: https://pubs.acs.org/10.1021/acs.energyfuels.3c01052

Notes

The authors declare no competing financial interest.

■ ACKNOWLEDGMENTS

This work was financed by the Swedish Research Council (2016-06023 and 2020-03487), Technical University of Denmark, Sino-Danish Center for Education and Research, and by Nordic Energy Research (project: NEST—Nordic Network in Solid Fuels towards Future Energy Systems, 120626). I. Adánez-Rubio acknowledges "Juan de la Cierva" Program (Grant IJC2019-038987-I funded by MCIN/AEI/10.13039/501100011033). Daofeng Mei is gratefully acknowledged for his help with the activation of the material.

■ NOMENCLATURE

CCS = carbon capture and storage
BECCS = bio-energy with carbon capture and storage
CLC = chemical looping combustion
AR = air reactor
FR = fuel reactor
OC = oxygen carrier
OCAC = oxygen carrier-aided combustion
XRD = X-ray diffractometry
BET = Brunauer−Emmett−Teller
SEM−EDX = scanning electron microscopy coupled with an energy-dispersive X-ray spectroscopy
SF = zinc saturation fraction

■ REFERENCES

(1) Gasser, T.; Guivarch, C.; Tachiiri, K.; Jones, C. D.; Ciais, P. Negative emissions physically needed to keep global warming below 2 °C. *Nat. Commun.* **2015**, *6*, No. 7958.

(2) Smith, P.; Davis, S. J.; Creutzig, F.; Fuss, S.; Minx, J.; Gabrielle, B.; Kato, E.; Jackson, R. B.; Cowie, A.; Kriegler, E.; et al. Biophysical and economic limits to negative CO2 emissions. *Nat. Clim. Change* **2016**, *6*, 42−50.

(3) Armstrong McKay, D. I.; Staal, A.; Abrams, J. F.; Winkelmann, R.; Sakschewski, B.; Loriani, S.; Fetzer, I.; Cornell, S. E.; Rockström, J.; Lenton, T. M. Exceeding 1.5C global warming could trigger multiple climate tipping points. *Science* **2022**, *377*, No. 7950.

(4) Rockström, J.; Gaffney, O.; Rogelj, J.; Meinshausen, M.; Nakicenovic, N.; Schellnhuber, H. J. A roadmap for rapid decarbonization. *Science* **2017**, *355*, 1269−1271.

(5) Smith, S. M.; Geden, O.; Nemet, G. F.; Gidden, M. J.; Lamb, W. F.; Powis, C.; Bellamy, R.; Callaghan, M. W.; Cowie, A.; Cox, E. et al. *The State of Carbon Dioxide Removal*, 1st ed.; CDR, 2023.

(6) Kemper, J. Biomass and carbon dioxide capture and storage: A review. *Int. J. Greenhouse Gas Control* **2015**, *40*, 401−430.

(7) Farooqui, A.; Bose, A.; Ferrero, D.; Llorca, J.; Santarelli, M. Techno-economic and exergetic assessment of an oxy-fuel power plant fueled by syngas produced by chemical looping CO2 and H2O dissociation. *J. CO2 Util.* **2018**, *27*, 500−517.

(8) Coppola, A.; Scala, F. Chemical Looping for Combustion of Solid Biomass: A Review. *Energy Fuels* **2021**, *35*, 19248−19265.

(9) Abanades, J. C.; Arias, B.; Lyngfelt, A.; Mattisson, T.; Wiley, D. E.; Li, H.; Ho, M. T.; Mangano, E.; Brandani, S. Emerging CO2 capture systems. *Int. J. Greenhouse Gas Control* **2015**, *40*, 126−166.

(10) Di Giuliano, A.; Capone, S.; Anatone, M.; Gallucci, K. Chemical Looping Combustion and Gasification: A Review and a Focus on European Research Projects. *Ind. Eng. Chem. Res.* **2022**, *61*, 14403−14432.

(11) Lind, F.; Corcoran, A.; Andersson, B.; Thunman, H. 12,000 Hours of Operation with Oxygen-Carriers in Industrially Relevant Scale (75,000 kWth). *VGB PowerTech J.* **2017**, *7*, 82−87.

(12) Moldenhauer, P.; Gyllén, A.; Thunman, H.; Lind, F. In *A Scale-Up Project for Operating a 115 MWth Biomass-Fired CFB boiler with Oxygen Carriers as Bed Material*, Proceedings of the 5th International Conference on Chemical Looping, 2018.

(13) Elled, A.-L.; Åmand, L.-E.; Eskilsson, D. Fate of Zinc during Combustion of Demolition Wood in a Fluidized Bed Boiler. *Energy Fuels* **2008**, *22*, 1519−1526.
(14) Staničić, I.; Backman, R.; Cao, Y.; Rydén, M.; Aronsson, J.; Mattisson, T. Fate of trace elements in Oxygen Carrier Aided Combustion (OCAC) of municipal solid waste. *Fuel* **2021**, No. 122551.
(15) Staničić, I.; Brorsson, J.; Hellman, A.; Mattisson, T.; Backman, R. Thermodynamic Analysis on the Fate of Ash Elements in Chemical Looping Combustion of Solid Fuels-Iron-Based Oxygen Carriers. *Energy Fuels* **2022**, *36*, 9648−9659.
(16) Khandelwal, H.; Dhar, H.; Thalla, A. K.; Kumar, S. Application of life cycle assessment in municipal solid waste management: A worldwide critical review. *J. Cleaner Prod.* **2019**, *209*, 630−654.
(17) Sharma, K. D.; Jain, S. Municipal solid waste generation, composition, and management: the global scenario. *Soc. Responsib. J.* **2020**, *16*, 917−948.
(18) Hoornweg, D.; Bhada-Tata, P.; Kennedy, C. Environment: Waste production must peak this century. *Nature* **2013**, *502*, 615−617.
(19) Khandelwal, H.; Thalla, A. K.; Kumar, S.; Kumar, R. Life cycle assessment of municipal solid waste management options for India. *Bioresour. Technol.* **2019**, *288*, No. 121515.
(20) Staničić, I.; Mattisson, T.; Backman, R.; Cao, Y.; Rydén, M. Oxygen carrier aided combustion (OCAC) of two waste fuels—Experimental and theoretical study of the interaction between ilmenite and zinc, copper and lead. *Biomass Bioenergy* **2021**, *148*, No. 106060.
(21) Thunman, H.; Lind, F.; Breitholtz, C.; Berguerand, N.; Seemann, M. Using an oxygen-carrier as bed material for combustion of biomass in a 12-MWth circulating fluidized-bed boiler. *Fuel* **2013**, *113*, 300−309.
(22) Berdugo Vilches, T.; Lind, F.; Rydén, M.; Thunman, H. Experience of more than 1000 h of operation with oxygen carriers and solid biomass at large scale. *Appl. Energy* **2017**, *190*, 1174−1183.
(23) Garcia, E.; Liu, H. Ilmenite as alternative bed material for the combustion of coal and biomass blends in a fluidised bed combustor to improve combustion performance and reduce agglomeration tendency. *Energy* **2022**, *239*, No. 121913.
(24) Schneider, T.; Krumrein, J.; Müller, D.; Karl, J. Investigation of the Oxygen Supply and Distribution in a Bubbling Fluidized Bed by Using Natural Ilmenite for Oxygen Carrier Aided Combustion. *Energy Fuels* **2021**, *35*, 12352−12366.
(25) Linderholm, C.; Schmitz, M.; Knutsson, P.; Lyngfelt, A. Chemical-looping combustion in a 100-kW unit using a mixture of ilmenite and manganese ore as oxygen carrier. *Fuel* **2016**, *166*, 533−542.
(26) Bartocci, P.; Abad, A.; Flores, A. C.; Loscertales, M. D. Ilmenite: A promising oxygen carrier for the scale-up of chemical looping. *Fuel* **2023**, *337*, No. 126644.
(27) Vigoureux, M.; Knutsson, P.; Lind, F. Sulfur Uptake during Oxygen-Carrier-Aided Combustion with Ilmenite. *Energy Fuels* **2020**, *34*, 7735−7742.
(28) Corcoran, A.; Marinkovic, J.; Lind, F.; Thunman, H.; Knutsson, P.; Seemann, M. Ash properties of ilmenite used as bed material for combustion of biomass in a circulating fluidized bed boiler. *Energy Fuels* **2014**, *28*, 7672−7679.
(29) Corcoran, A.; Knutsson, P.; Lind, F.; Thunman, H. Mechanism for migration and layer growth of biomass ash on ilmenite used for oxygen carrier aided combustion. *Energy Fuels* **2018**, *32*, 8845−8856.
(30) Gyllén, A.; Knutsson, P.; Lind, F.; Thunman, H. Magnetic separation of ilmenite used as oxygen carrier during combustion of biomass and the effect of ash layer buildup on its activity and mechanical strength. *Fuel* **2020**, *269*, No. 117470.
(31) Knutsson, P.; Linderholm, C. Characterization of ilmenite used as oxygen carrier in a 100 kW chemical-looping combustor for solid fuels. *Appl. Energy* **2015**, *157*, 368−373.
(32) Adánez, J.; Cuadrat, A.; Abad, A.; Gayán, P.; Diego, L. F. D.; García-Labiano, F. Ilmenite activation during consecutive redox cycles in chemical-looping combustion. *Energy Fuels* **2010**, *24*, 1402−1413.
(33) Miya, K.; Otomo, J. Improvements in reaction kinetics and stability of ilmenite as oxygen carrier by surface modification with calcium titanate in redox cycles of chemical-looping systems. *Chem. Eng. J.* **2017**, *327*, 257−267.
(34) Leion, H.; Frick, V.; Hildor, F. Experimental Method and Setup for Laboratory Fluidized Bed Reactor Testing. *Energies* **2018**, *11*, 2505.
(35) Schwebel, G. L.; Leion, H.; Krumm, W. Comparison of natural ilmenites as oxygen carriers in chemical-looping combustion and influence of water gas shift reaction on gas composition. *Chem. Eng. Res. Des.* **2012**, *90*, 1351−1360.
(36) Bale, C. W.; Bélisle, E.; Chartrand, P.; Decterov, S. A.; Eriksson, G.; Gheribi, A. E.; Hack, K.; Jung, I. H.; Kang, Y. B.; Melançon, J.; et al. FactSage Thermochemical Software and Databases—2010−2016. *Calphad* **2016**, *54*, 35−53.
(37) Staničić, I.; Backman, R.; Cao, Y.; Rydén, M.; Aronsson, J.; Mattisson, T. Fate of trace elements in Oxygen Carrier Aided Combustion (OCAC) of municipal solid waste. *Fuel* **2022**, *311*, No. 122551.
(38) Jones, F.; Tran, H.; Lindberg, D.; Zhao, L.; Hupa, M. Thermal Stability of Zinc Compounds. *Energy Fuels* **2013**, *27*, 5663−5669.
(39) Nielsen, A. R.; Larsen, M. B.; Glarborg, P.; Dam-Johansen, K. High-Temperature Release of SO2 from Calcined Cement Raw Materials. *Energy Fuels* **2011**, *25*, 2917−2926.
(40) Yan, Z.; Wang, Z.; Liu, H.; Tu, Y.; Yang, W.; Zeng, H.; Qiu, J. Decomposition and solid reactions of calcium sulfate doped with SiO2, Fe2O3 and Al2O3. *J. Anal. Appl. Pyrolysis* **2015**, *113*, 491−498.
(41) Zhang, S.; Shi, R.; Tan, Y. Comparison of the Solubility of ZnFe2O4, Fe3O4 and Fe2O3 in High Temperature Water. *J. Solution Chem.* **2018**, *47*, 1112−1126.

https://doi.org/10.1021/acs.energyfuels.3c01052
Energy Fuels 2023, 37, 7856−7870